Charge and spin transport over record distances in GaAs metallic n-type nanowires

H. Hijazi[1], D. Paget[2], G. Monier[1], G. Grégoire[1], J. Leymarie[1], E. Gil[1], F. Cadiz[2], C. Robert-Goumet[1], and Y. André[1]
[1] *Université Clermont Auvergne, CNRS, SIGMA Clermont, Institut Pascal, F-63000 Clermont-Ferrand, France and*
[2] *Physique de la matière condensée, Ecole Polytechnique, CNRS, IP Paris, 91128 Palaiseau, France*
(Dated: May 13, 2021)

We have investigated charge and spin transport in n-type metallic GaAs nanowires ($\approx 10^{17}$ cm^{-3} doping level), grown by hydride vapor phase epitaxy (HVPE) on Si substrates. For this doping level, charge and spin transport might appear difficult because of the expected localization of minority holes in the valence band potential fluctuations generated by statistical fluctuations of the donor concentration. In contrast with these expectations, it is found, using spatially- and spectrally-resolved investigation of the luminescence intensity and circular polarization under laser excitation, that i) establishment of a charge thermodynamic equilibrium between the photoelectrons and the Fermi sea occurs over a distance from the excitation spot of 2 μm. At this distance, the spin polarization is still observed, implying that photoelectrons have preserved their spin orientation and that the two spin reservoirs remain distinct. ii) Charge can be transported over record distances larger than 20 μm at 6K. iii) Spatially-resolved investigations show that a photoelectron spin polarization of 20% can even be transported over a record distance of more than 20 μm. This long distance transport occurs because of the presence of large internal electric fields of ambipolar origin, further enhanced by the spatial redistribution of the Fermi sea. These findings has potential applications for long distance spin transport in n-type doped nanowires.

I. INTRODUCTION

The investigation of transport in systems of reduced dimensionality such as nanowires (NWs) is of interest both for fundamental reasons and for applications to solar cells [1], lasers [2], quantum computing [3] and spintronics. In silicon, time-resolved experiments have shown that photocarriers can be transported over ≈ 1 μm [4]. For GaAs, the largest charge diffusion length is of 4 μm at LT in quantum NWs [5]. However, most reported values at LT [6–9] and RT [10] are in the submicron range. Finally, spin transport has to our knowledge been little investigated.

N-type GaAs NWs on the metallic side of the Mott transition appear as a promising system for spin transport because of the large spin lifetime [11, 12]. The efficiency of the Dyakonov-Perel process, which is dominant at this doping level, is likely to be further reduced if the axial NW direction is <111>, since the latter process is inefficient if the k vector lies along <111> [13]. A spin diffusion length as large as 10 μm has been reported for bulk n- type GaAs on the insulating side of the transition [14].

At this doping level, there appear tails in the valence and conduction band, due to statistical fluctuations of donor concentration [15–17]. Investigations have considered luminescence analysis of bulk samples [18], as well as transport of majority carriers on bulk materials, using macroscopic tools such as conductivity measurements [19–21]. It has been predicted that disorder in one dimensional semiconducting systems can lead to freezing of the spin relaxation [22]. On the other hand, because of the efficient relaxation of the hole kinetic energy [23, 24] and because of the difficulty of holes to undergo tunnel processes due to their large effective mass [18], holes may stay trapped in the potential fluctuations. This may strongly reduce the distance over which minority carriers can be transported.

In the present work, we use metallic NWs of $\approx 10^{17}$ cm^{-3} doping level, of exceptional quality and length, produced using Hydride Vapor Phase Epitaxy [25–27]. The NW is excited by a tightly-focussed circularly-polarized laser and the luminescence intensity and polarization are monitored at 6K with spatial resolution along the NW [28]. This allows us to investigate charge and spin transport along the NW. As shown before [29], this approach has similarities with time-resolved luminescence investigations [30], but is more appropriate to describe charge and spin transport.

We show that, for these NWs and, at variance with the expected localization of minority carriers, NWs on the metallic side of the Mott transition appear as very promising candidates for charge and spin transport. This is due to the buildup of large internal electric fields of ambipolar origin, which themselves induce a redistribution of the Fermi sea. These electric fields increase the hole mobility, so that minority holes can be transported in the bandtails over lengths as large as 20 μm. Photoelectrons are also transported over similar distances, without loss of their spin oritentation, so that a spin polarization as large as 20 % is measured at such large distance.

In the same way as for electrolyte cells with which the present system has close analogies[31], several phases appear in the spatial profiles, which depend on excitation power. These phases are caused by the appearance of an excess of charge in the Fermi sea near the excitation spot, along with a depletion at a distance, depending on excitation power, between 2 and 10 μm.

We also investigate, as performed before for bulk materials [32] and heterostructures [33], to what level the

presence of a Fermi sea of spin-unpolarized intrinsic electrons affects charge and spin transport in the NW. It is shown that thermodynamic equilibrium between photoelectrons and the Fermi sea is established after a small distance of 2 μm, but that the two spin reservoirs remain distinct up to 20 μm.

This paper is organized as follows. The following section is devoted to a background on transport in NW's and to experimental aspects. Sec. III is devoted to experimental analysis of the establishment of a charge equilibrium between photoelectrons and the Fermi sea. Sec. IV contains an experimental analysis of the spatial profiles, and its interpretation using the spatial distribution of internal electric field and of the Fermi sea. In Sec. V, we present an investigation of spin transport along the NW, while Sec. VI contains a discussion of the various spatial phases which appear in the NW.

II. PRINCIPLES

A. NW growth and preparation

Here, we study gold-catalyzed NWs, HVPE-grown on Si(111) substrates at 715 °C. These NWs have a length of several tens of μm and are characterized by a pure zinc blende structure, free of polytypism and cristalline defects [25, 26]. Since the HCl flux injected inside the reactor produces $SiCl_4$ which acts as a doping precursor, the NW have a donor doping level N_D in the low 10^{17} cm^{-3} range, weakly dependent on NW diameter [27]. This value has been obtained from an analysis of the shape of the luminescence spectrum, by Raman analysis [34] and using a mapping of the luminescence intensity **(see supplemental material, section I (SM-I) at [35] and references [27, 36, 37] therein for more details about doping level estimate)**. This value is about one order of magnitude larger than the one of the Mott transition [19–21].

Immediately after growth, the NW were capped with a thin layer of nitride at the GaAs surface which reduces the surface oxidation under air exposure and decreases the surface recombination velocity [38, 39]. This was performed by introduction without air exposure into a UHV chamber and treatment at 300K by a nitrogen plasma produced by a commercial electron cyclotron resonance source (SPECS MPS-ECR) operating in atom mode at a pressure of $2.5.10^{-5}$ mbar and described elsewhere [40]. In order to obtain a homogeneous nitridation on the NW surface, the angle between the source and the substrate surface was kept at 45° for 1h and at -45° for 1h.

The NWs, standing on the substrate, were mechanically deposited horizontally on a grid of lattice spacing 15 μm. An optical microscope was used to note the coordinates of the individual NW. As found by scanning electron microscopy, the NW used here had a length of 80 μm and a diameter of $\approx$ 220 nm. Since for this doping level, the width of the surface depletion region is of the order of 90nm, this leaves a central undepleted region of diameter $\approx$ 40 nm, from which the luminescence is detected.

B. Background on luminescence of metallic n-type GaAs

In a sphere of radius R, the statistical fluctuation of the mean number of donors N, given by $N = 4\pi N_D/(3R^3)$, is $\sqrt{N}$, so that the potential fluctuation is $\sqrt{N}q^2/(\epsilon\epsilon_0 R)$ where ϵ is the static dielectric constant, ϵ_0 is the permittivity of vacuum and q is the absolute value of the electronic charge [15]. These potential fluctuations result in spatial fluctuations of the bottom of the conduction band and of the top of the valence band. These fluctuations are screened by mobile carriers. Within the Thomas Fermi (TF) 3D model the screening concerns fluctuations of extension larger than $r_s = (1/2)\sqrt{a_0^* N_D^{1/3}} \approx a_0^*$ where a_0^* is the donor Bohr radius [41–43].

For $N_D \approx 10^{15}$ cm^{-3}, one merely observes a broadening of the donor band [44]. In contrast, for the present doping level $N_D \approx 10^{17}$ cm^{-3}, the fluctuations generate a tail lying lower than the conduction band (see left panel of Fig. 1). The amplitude of this tail is of the order of $\Delta E_c \approx 8\ meV$, i. e. comparable with the donor binding energy, while the density of states $\rho_c(\epsilon_c)$ increases linearly as a function of energy ϵ_c with respect to the bottom of the tail [44]. The valence band also exhibits a tail of amplitude $\Delta E_v \approx 8$ meV, with a density of states $\rho_v(\epsilon_v)$ increasing also linearly with increasing energy with respect to the top of the tail ϵ_v.

A key specificity of semiconductors near the metal-insulator transition under light excitation is that the dynamic properties of the two types of carriers in the fluctuations are very different [18, 45]. For electrons, because of the small effective mass, diffusion by tunnel processes from one well to the other one is quite efficient. Thus, the electronic reservoir is characterized by a thermodynamic equilibrium defined by a quasi Fermi level. The fact that the NW is metallic implies that elctrons at the Fermi level are mobile, so that the mobility level which defines the limit between mobile and trapped electrons, lies below E_F.

On the other hand, photoholes tend to get trapped in the potential wells, since relaxation of their kinetic energy occurs in a short characteristic time of 1 ps [23, 24], where tunneling processes are less probable because of their large effective mass.

The characteristics of recombination in this disordered system are described in Appendix. At a given radial r and axial position z in the NW, the intensity, obtained by integration of Eq. A3 over energy E, is of the form

$$I_{main} = K n_0 p. \tag{1}$$

where K is the bimolecular recombination constant. In the same way, the intensity of the emission due to recom-

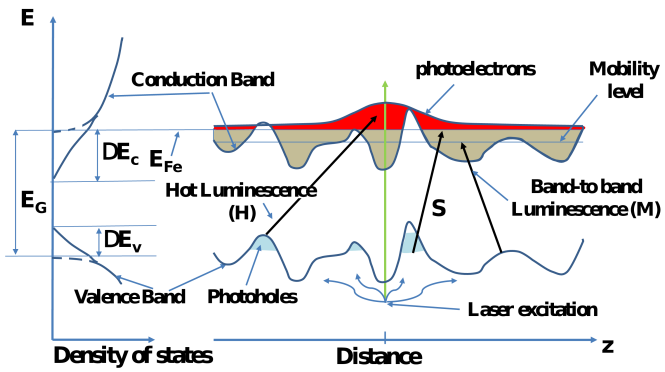


FIG. 1. Scheme for carrier excitation in the potential fluctuations of the conduction and valence bands of n-doped NW. Intrinsic electrons occupy the fluctuations of the conduction band up to the quasi Fermi level E_{Fe}. With the value of the doping level, this Fermi level lies above the mobility level, above which the electrons are no longer confined and participate to the electric conductivity. The various nearbandgap emissions are labelled in the same way as in the spectra of Fig. 3.

bination between photoelectrons and photoholes is

$$I_{hot} = K_{hot} np. \tag{2}$$

where K_{hot} is the corresponding bimolecular recombination constant. The detected luminescence intensity at a given axial position z along the NW is obtained by averaging over the radial coordinate r.

C. Conservation equations for charge transport

As shown in Ref. [46], even for hopping transport, it is possible to define effective mobilities and diffusion constants. Charge transport in the NW is described by two conservation equations. The first one is the diffusion equation for minority holes

$$g - K n_0 p - K_{hot} np - \frac{p}{\tau_{nr}} + \vec{\nabla}[D_h \vec{\nabla} p + \mu_h p \vec{E}] = 0. \tag{3}$$

Here g is the rate of creation of electron-hole pairs, τ_{nr} is the nonradiative recombination time, D_h is the hole diffusion constant, μ_h is the hole mobility and $\vec{E}$ is the internal electric field. The electron diffusion equation is

$$g - K n_0 p - K_{hot} np - \frac{n}{\tau_{nr}} + \vec{\nabla}[D_e \vec{\nabla}(n + \delta n_0) + \mu_e (n + n_0^*)\vec{E}] = 0, \tag{4}$$

where D_e is the diffusion constant and μ_e is the electron mobility. This equation expresses the known fact [47] that the diffusive current concerns the departure from equilibrium of the total electron concentration, where $\delta n_0 = n_0 - N_D$ is the light-induced change of the concentration of intrinsic electrons. The drift current concerns the photoelectrons and the fraction of the Fermi sea, which can participate to drift currents, of concentration $n_0^* \approx n_0 k_B T_e / E_{Fe}$. Here q is the absolute value of the electron charge, k_B is Boltzmann's constant and E_{Fe} is the electron Fermi energy and T_e is the electron temperature. If, in Eq. 3, the internal electric field $\vec{E}$ is negligible, hole diffusion is unipolar and is decoupled from electron diffusion. Resolution of the resulting equation for a NW leads in the present case to a featureless exponential decay of photocarrier concentration, as shown in **SM-II [48] (see, also, references [29, 49] therein)**.

It is however known that electrostatic interaction between mobile negative and positive charges [47, 50–52] can lead to nonexponential intensity spatial profiles [53]. Comparison of Eq. 3 and Eq. 4 gives the ambipolar electric field

$$\vec{E_a} = \frac{(D_h - D_e)\vec{\nabla} p}{\mu_e (n + n_0^*) + \mu_h p} + \frac{D_e \vec{\nabla}(n + \delta n_0 - p)}{\mu_e (n + n_0^*) + \mu_h p} \tag{5}$$

This equation allows us to write Eq. 3 as a drift-diffusion equation with an ambipolar diffusion constant given by

$$D_a = \frac{\mu_e (n + n_0^*) D_h + \mu_h p D_e}{\mu_e (n + n_0^*) + \mu_h p} \tag{6}$$

The effective diffusion length is $L_a = \sqrt{D_a \tau_h}$, where the hole lifetime τ_h is given by $1/\tau_h = K_{hot} n + K n_0 + 1/\tau_{nr}$.

D. Experimental

The experimental setup is sketched in Fig. 2. The excitation light is a tightly-focused, continuous-wave, laser beam (Gaussian radius $\sigma \approx 0.6$ μm, energy 1.59 eV). The luminescence light is focused on the entrance slit of a spectrometer equipped with a CCD camera as a detector.

For spatially-resolved spectral analysis, one monitors the image from the CCD detector. A typical image, taken for a NW temperature of 6K, is shown in Fig. 2 for an excitation power of 9 μW [54]. Here, the NW is adjusted so that its image by the detection optics is parallel to the spectrometer entrance slit (axis Z). Thus, section of the image along the perpendicular axis X gives the luminescence spectrum at the corresponding position on the NW. In the same way, section of the image along an axis parallel to Z gives the spatial profile of the emission at the corresponding energy. As shown in Fig. 2 and in agreement with previous work [28], the spatial profiles extend well beyond the zone of optical excitation (≈ 0.6 μm), so that the monitoring of the emission as a function of distance gives information on evolution of the photocarrier charge and spin reservoirs during transport away from the excitation spot.

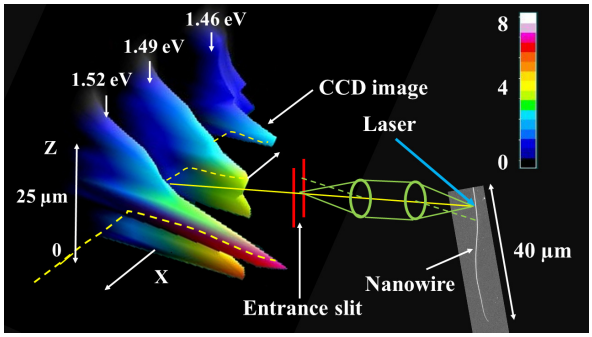


FIG. 2. Scheme of the experimental setup, showing a scanning electron microscope picture of the NW and a 3D picture of the CCD image at 6K for an excitation power of 9 μW. The image exhibits 3 main emissions, including the nearbandgap luminescence near 1.52 eV and two less intense bands due to recombination at residual acceptors. Section of this image along the X axis, perpendicular to the entrance slit (dotted curve), gives the luminescence spectrum at a given position in the NW.

Liquid crystal modulators were used to circularly-polarize the excitation laser ($\sigma^{\pm}$-helicity), in order to generate spin-polarized photoelectrons and to selectively detect the intensity $I(\sigma^{\pm})$ of the luminescence components with $\sigma^{\pm}$ helicity. Since photoholes as well as intrinsic electrons are spin-unpolarized, the band-to-band luminescence is expected to be also circularly-unpolarized. Conversely, for recombination with spin-polarized photoelectrons, one monitors the difference signal

$$I_D = I_{hot}(\sigma^+) - I_{hot}(\sigma^-) = K_{hot}\mathscr{P}_i s. \qquad (7)$$

where $\mathscr{P}_i = \mp 0.5$ for $\sigma^{\pm}$- polarized excitation. This signal is related to the photoelectron spin density $s = n_+ - n_-$, where $n_{\pm}$ are the concentrations of photoelectrons with spin $\pm 1/2$, choosing the direction of light excitation as the quantization axis. Finally, the ratio $\mathscr{P} = I_D/I_S$ is defined as the degree of circular polarization of the luminescence and is $\mathscr{P} = \mathscr{P}_i s/n$.

The luminescence image shown in Fig. 2 consists in three bands. The band related at 1.49 eV is due to residual carbon acceptors [55, 56]. The band near 1.46 eV, possibly caused by carbon acceptors perturbed by nitrogen atoms originating from the surface passivation [57, 58] has properties very close to the former one. Investigation of the spectral and spatial properties of these emissions can be found in the **SM-III at [59] (see, also, references [18, 41, 55–58, 60, 61])**. Analysis of the nearbandgap emission is performed in the following section.

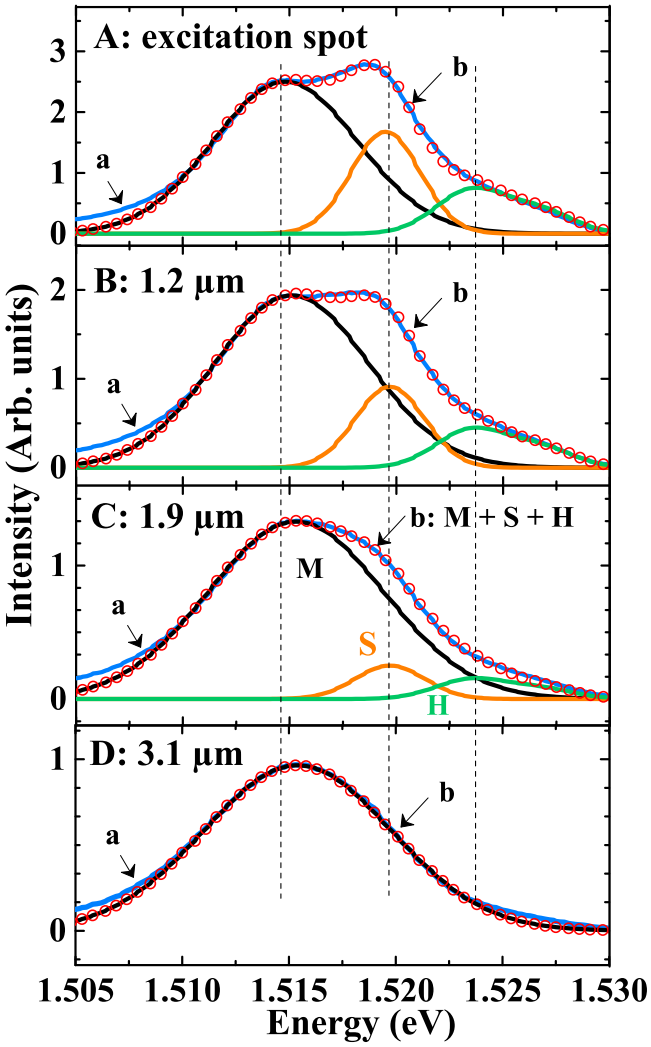


FIG. 3. Spatially-resolved spectra (Curves a) at the excitation spot (A) and for selected distances from this spot of 1.2 μm (B), 1.9 μm (C) and 3.1 μm (D), for an excitation power of 45 μW. All the spectra were decomposed using the main component (M), the shoulder at 1.519 eV (S) and the hot electron contribution (H). Curves b show the sum of these contributions and closely follow the experimental spectra.

III. SPECTRAL AND SPATIAL CHARACTERISTICS OF THE NEARBANDGAP EMISSION

Fig. 3 shows the intensity spectra for an excitation power of 45 μW and for selected distances to the excitation spot. The present section contains a qualitative analysis of the spectrum at $z = 0$, shown in Panel A. Quantitative analysis can be found in the Appendix. This spectrum is composed of a main line near 1.515 eV labelled M, of a shoulder at 1.519 eV labelled S and of a high-energy tail, above 1.52 eV, labelled H.

A first indication on the nature of these lines is given by their degree of circular polarization. Fig. 4 shows

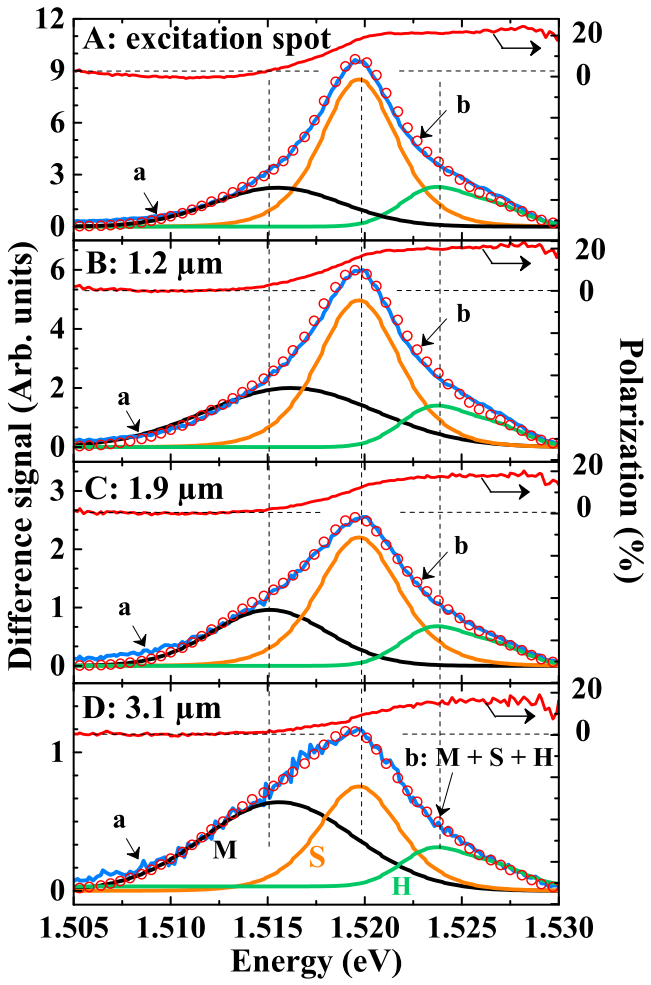


FIG. 4. Same as Fig. 3, but for the difference spectra. Also shown are the polarization spectra, defined as the ratio between difference signal and intensity. Note that, at large distance (Panel D), component S is still the dominant feature of the difference spectrum, whhile it has disapeared from the corresponding intensity spectrum .

the difference spectra in the same conditions as Fig. 3 as well as, for each distance, the polarization spectra. The spectrum shown in Panel A of Fig. 4 exhibits, as already reported before [11], a weak polarization of the M line. This is because line M is due to recombination of spin-unpolarized photoholes with intrinsic electrons. Indeed, because of band filling, electrons lying below the Fermi level cannot be spin-polarized. Conversely, lines S and H are polarized and are therefore due to recombination of spin-polarized photoelectrons at the photoelectron quasi-Fermi level and above this level, respectively. This interpretation is confirmed by the power dependence of the intensities of these lines (Appendix A), according to which, in agreement with Eq. (1), the intensity of line M is proportional to excitation power, while, according to Eq. (2), that of line H is proportional to the square of this power.

Such fine structure of the nearbandgap emission has already been reported, mostly for pure GaAs, where a line similar to line S has been attributed to excitons, or biexcitons [41, 62–64]. Because of screening of the electron-hole interaction, this structure strongly decreases upon increasing doping, since the exciton absorption peak disappears for $N_D > 10^{16}\ cm^{-3}$ [65]. For more doped materials, a relatively weak shoulder at a slightly higher energy of 1.525 eV has been reported [41], and tentatively attributed to a Fermi edge singularity [17, 66].

However, these interpretations do not hold for the present case. This is shown using a simple spatially-resolved spectral experiment, which leads to the conclusion that line S is only visible in the vicinity of the excitation spot. Shown in the top panel of Fig. 5 are the intensity spatial profiles of line M for increasing excitation powers, but without any normalization. While discussion of these profiles is postponed to Sec. IV, it is noted here that the emission intensity of Curve a at $z = 0$ is the same as for Curve b at $z = 4.9$ μm. and for Curve c at $z = 14.5$ μm. These three situations, marked by arrows in Fig. 5, correpond then to similar photoelectron and minority hole concentrations and only differ by the distance to the excitation spot. If line S was caused by recombination of one of the electronic species described above, one would expect to observe similar magnitudes of line S. Such hypothesis is contradicted by the experiment. As shown in the bottom panel, although lines M and H are very similar for the three spectra and nearly disappear in the difference a-c, line S is only observed at $z = 0$.

These results show that line S is a transient spatial feature occuring during transport away from the excitation spot and reflecting irreversible establishment of equilibrium occuring after generation of electron-hole pairs. This equilibrium concerns the photoelectron gas since the hole energy relaxation time is quite short and smaller than 1 ps [23] and since establishment of equilibrium among the hole gas would also affect line M.

For quantitative analysis, the spectra were decomposed into elementary contributions, as discussed in Appendix and also shown in Fig. 3. One sees that line S disappears over a characteristic distance of ≈ 2 μm so that the spectrum shown in Panel D mostly exhibits line M, with a weak residual H signal above 1.52 eV. The spatial profiles of line S are shown in Fig. 6 for several excitation powers. The decay is slower than that of the laser spatial profile, shown in Curve d of Fig. 6, implying that the spatial dependence of these spectra are not directly related to the photocarrier creation rate but to evolution of the photocarrier system during transport. As seen from Fig. 6, the characteristic distance for establishment of equilibrium relatively weakly depends on excitation power and increases by less than a factor of 2 between Curves a and c, while the excitation power has increased by two orders of magnitude. The fact that the resulting increase of the heat capacitance of the photoelectron reservoir has little effect on the photoelectron dynamics suggests that, even for the maximum power, the photoelectron concentration

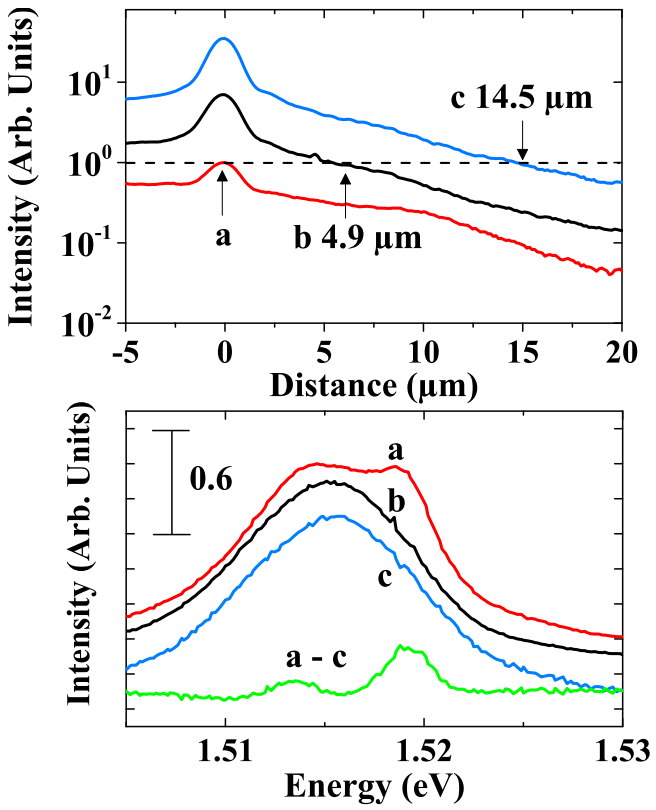


FIG. 5. The top panel shows the spatial profiles of the near-bandgap line for an excitation power of 9 μW (Curve a), of 45 μW (Curve b), and 180 μW (Curve c). The emission intensity of Curve b(c) is the same as that of Curve a at $z = 0$, but for $z = 4.9(14.5)$ μm. These three situations correpond then to similar photoelectron and minority hole concentrations. The bottom panel shows the corresponding nearbandgap luminescence spectra. Line S is only seen near the excitation spot. This shows that line S reflects establishment of equilibrium during photoelectron diffusive transport rather than luminescence from an electronic species such as excitons.

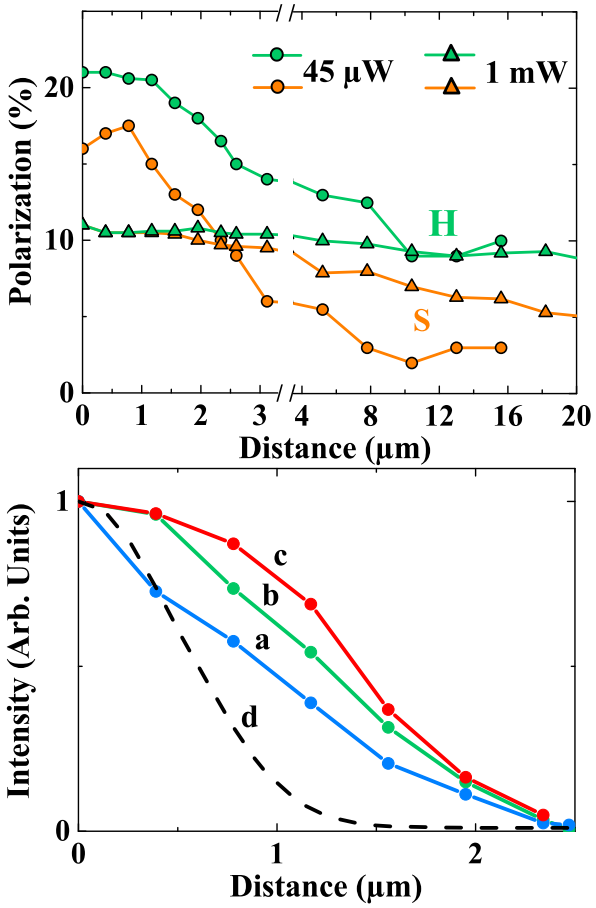


FIG. 6. The bottom panel shows the spatial profiles of the intensity of line S in the intensity spectra, obtained using the decomposition shown in Fig. 3, for an excitation power of 9 μW (Curve a), 45 μW (Curve b) and 1 mW (Curve c). This decay reveals the establishment of thermodynamic equilibrium between photoelectrons and intrinsic electrons. Also shown in Curve d is the laser intensity spatial profile. The top panel shows the spatial profiles of the degree of circular polarization for line H and line S for an excitation power of 45 μW (circles) and 1 mW (triangles).

is smaller than that of the Fermi sea. The slowing down of the interaction between the two types of reservoirs could be caused by screening of the interactions between electrons by mobile charges [67].

In order to interpret these results, it is recalled that the first dynamic process which occurs after creation of an electron in the conduction band is emission of an optical phonon. This emission has been found to occur in a time of ≈ 0.2 ps [68]. Although this time may be larger at high excitation power because of screening of the electron-phonon interaction [69], the observation of a significant S signal at $z = 0$ suggests that emission of optical phonons is complete before diffusion out of the excitation spot.

Electron-electron collisions are known to enable efficient establishment of equilibrium among the electron gas. The time for collisions between electrons has been calculated including screening by an electron hole plasma and found smaller than 1ps independently on concentration and temperature, although the present values of concentration and temperature have not been considered [70]. Experimentally, the time for establishment of equilibrium between photoelectrons and a Fermi sea of electrons has been found to be shorter than 30 fs. However, this was found in a modulation-doped structure i.e. without screening by charged donors [32]. Thus it may be believed that establishment of equilibrium among photoelectrons occurs before they leave the excitation spot.

The present experimental results suggest that, in contrast, equilibrium between the photoelectrons and Fermi edge intrinsic electrons only occurs after a distance of 2 μm. The relatively slow establishment of equilibrium with the Fermi sea contradicts the reported fast establishment of equilibrium due to electron-electron collisions. This result is not completely understood and its explana-

tion requires further theoretical analysis. However, the present slow establishment is consistent with investigations under transport, according to which the interaction between photoelectrons and the Fermi sea, rather than occuring through single particle processes, modifies the equilibrium of the overall Fermi sea [33]. Screening of the electron-electron interactions by donor charges may also play a role [67].

IV. CHARGE TRANSPORT ALONG THE NW

A. Results

Fig. 7 shows, for selected excitation powers, the spatial intensity profiles at 1.515 eV (Curves a, line M) and at 1.529 eV (Curves b, line H). The spatial profiles of line M exhibit a rapid decrease over a distance of 2 μm. Although this distance is slightly larger than the spatial extent of the laser (also shown in the bottom panel), the decay reveals that some holes are weakly diffusing and tend to recombine near the excitation spot. A key result is that the amplitude of this decrease is small at low excitation power, in which case, the profile is dominated by a slow tail. Since line M is due to recombination of minority holes with the Fermi sea, this implies that minority carriers have been transported away from the excitation zone over a distance as large as 20 μm. The relative amplitude of this decay decreases with increasing power so that, at the highest power, the amplitude of the tail is one order of magnitude smaller than the signal at $z = 0$.

Four distinct regimes, labelled I-IV in Panel C, can be distinguished. At the smallest excitation power (Curve a of Panel A), the weak decrease up to about 2 μm (Phase I) is followed by a slow exponential-like decay up to 11 μm from which we obtain an effective diffusion length of 10.8 μm (Phase II) and again a by faster one for larger distances (Phase III). The profile of line H does not exhibit the slow decay of Phase II. It consists mostly of a decay up to 2 μm, for which the amplitude is larger than that of Curves a, followed by a single exponential-like decay over the whole spatial range.

Increase of the excitation power only slightly affects the profile of line H, apart from the appearance of a faster decay beyond 20 μm (Phase IV, most visible in Panel D of Fig. 7). Upon increase of the excitation power, in addition to the increase of the amplitude of phase I, one sees that the slow decay of the intensity profile in phase II occurs over a progressively smaller distance and becomes faster. For the largest excitation power (Panel D), Phase II has completely disappeared and the profile consists of only phases I, III and IV.

B. Interpretation

The observation of band-to-band luminescence up to 25 μm implies long distance transport of photoholes and

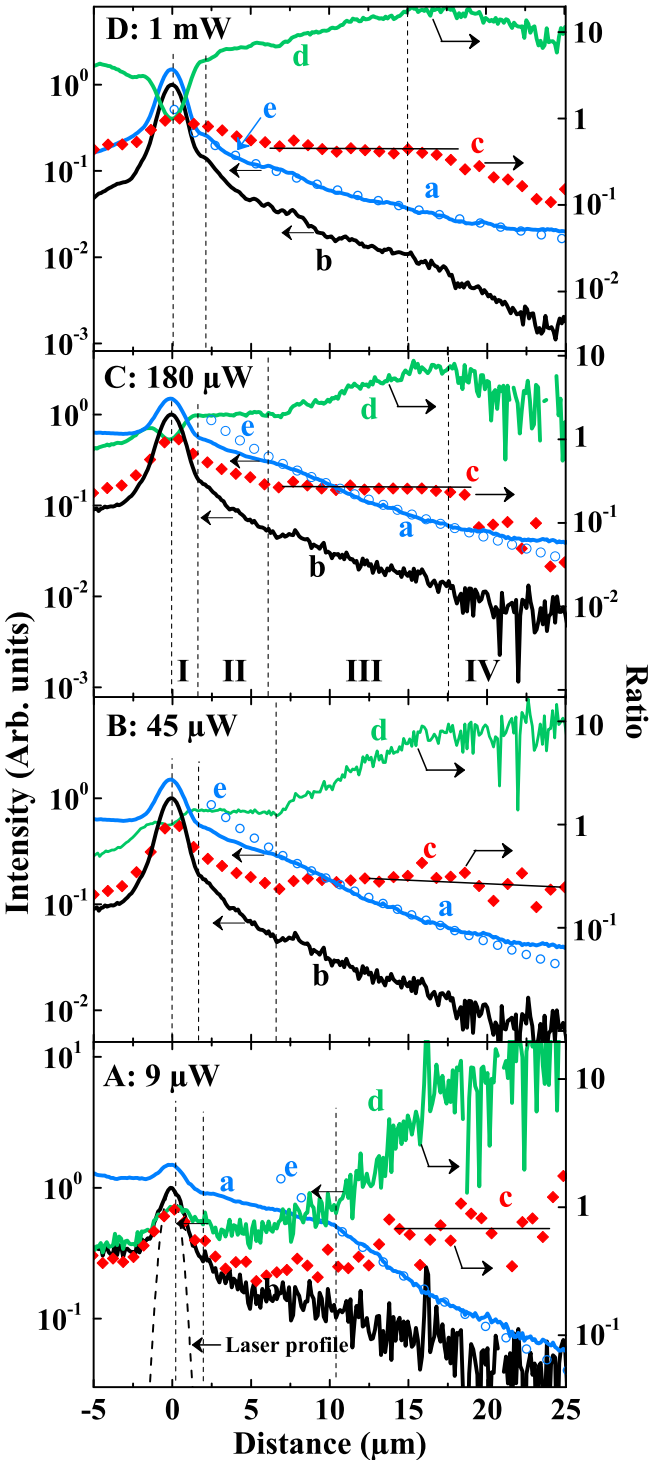


FIG. 7. Intensity spatial profiles of line M (1.515 eV, Curves a), of line H (1.527 eV, Curves b) for selected excitaton powers of 9 μW (A), 45 μW (B) 180 μW (C) and 1 mW (D). Each panel also shows the ratios $\mathscr{C}$ (Curves c) and $\mathscr{B}$ (Curves d), given by Eq. 13 and Eq. 12, respectively. Curves e are fits of Curve a using Eq. 14, describing ballistic hole transport over the fluctuations.

is in contradiction with the fact that the relaxation of the hole kinetic energy [23, 24] is more rapid than for electrons. This would imply that holes tend to accumulate in the potential wells, of height larger than the thermal energy, where tunneling processes are less probable than for electrons because of their large effective mass. Another possible mechanism of self-trapping of photoholes is caused by spatial inhomogeneneities of the surface photovoltage [71].

In order to resolve this contradiction, we can exclude a simple explanation implying photon-mediated transport, originating from laser or luminescence light channeling in the NW. Indeed, no light at the laser energy is found at the end of the NW, which is evidence that the excitation laser does not couple to guided modes in the NW. Some luminescence light may propagate along the NW and may be reabsorbed over a distance of the order of 1 μm. It could affect the spatial profile over longer distances if the newly-generated electron-hole pairs in turn emit photons (photon recycling). However, because of the matrix elements involved in these processes, emission of a photon in the same way as creation of a spin-polarized electron, occur with a loss of angular momentum by a factor of 2, so that spin recycling occurs with a loss of a factor of 4 and should create weakly spin-polarized electrons, in contradiction with the observation of long distance spin transport, reported in Sec. V.

Another effect to be excluded is the possible presence of thermoelectric charge and spin currents due to spatial inhomogeneities of the photoelectron temperature. The temperature spatial profiles, reported in **SM-IV [72] (see,also, reference [18] therein)**, show a very weak temperature spatial gradient at low excitation power. At the highest power, the gradients are very close to those reported before in similar experimental conditions [29]. Since the latter work has concluded that thermoelectric currents do not strongly contribute to the profiles, thermoelectric effects will be neglected here.

Thus, the intensity spatial profiles directly reflect photocarrier transport along the NW and should be described by Eq. 3 and Eq. 4. In the present case these equations can be simplified for two reasons. Firstly, although minute departures from neutrality are possible, caused by internal electric fields, it has been shown [50], that charge neutrality is valid so that

$$p \approx \delta n_0 + n \tag{8}$$

This implies that the second term of Eq. 5 can be neglected. Seconldy, taking a typical value of the diffusion constant of 100 cm$^2/s$ [29], the photocarrier concentration n at the excitation spot is of the order of 10^{14} cm $^{-3}$ for the weakest excitation power used below. The fact that the result is several orders of magnitude smaller than the doping level and the fact that possible departures from the monomolecular regime at the highest excitation power are not observed allow us to conclude that $n << n_0^* < N_D$ and $p << n_0^* < N_D$ throughout the excitation power range. In this case $D_a \approx D_h$ and $L_a = \sqrt{D_h \tau_h}$ so that unipolar diffusion takes place. As a result, the electric field can be approximated by

$$\vec{E_a} \approx \frac{(D_h - D_e)\vec{\nabla} p}{\mu_e n_0^* + \mu_h p} \tag{9}$$

This equation expresses the fact that the difference of hole and electron diffusive currents is equal to the difference of the corresponding drift currents. Assuming $D_e > D_h$, this field is directed outwards and proportionnal to the slope $\vec{\nabla} p$ of the nearbandgap line, for which the intensity is given by Eq. 1.

The field E_a given by Eq. 9 is evaluated using the Einstein relation, which is for a disordered sample $D_e = \mu_e \mathscr{E}/q$. The energy $\mathscr{E}$ is comparable with the fluctuation amplitude at low temperature and becomes equal to the usual value $k_B T_e$, if the temperature is increased [46]. One obtains $E_a \approx \mathscr{E} p/(q L_a n_0^*)$. This field is of the order of $10^{-3}(p/n_0^*)$ V/μm. This is several orders of magnitude smaller than typical electric fields in the fluctuations, of the order of the unscreened effective field near a donor $E_D/a_0^* \approx 0.6$ V/μm. As a result, usual ambipolar fields cannot affect photocarrier transport in the disordered NW.

It is now shown that, as already reported earlier experimentally [73], the presence of disorder may strongly increase the mobility and therefore the minority carrier drift length. Here, the potential fluctuations, rather than preventing transport, will result in a self-adjustment of the electric field to a value enabling tunnel processes and long distance transport.

Since thermal and electrical activation of the conductivity are of the same nature, and in the same way as for amorphous materials, the electric field dependence of the mobility is similar to that of the temperature dependence. This temperature dependence of the electron and hole conductivities is of the type $\sigma_{e(h)} = \sigma_{e(h)0} \exp\left[-\left(\Delta_{e(h)}/k_B T_{e(h)}\right)^{\beta}\right]$. Here, $\Delta_{e(h)}$ are activation energies and the exponent β is of the order of unity [19, 46]. The electric field dependence of the mobilities is then found by replacing in the above equation the thermal energy by $qE\delta$, where δ is the characteristic distance travelled in an elementary hopping process [46]. This distance can be larger than the typical dimension of the fluctuation, of the order of the donor Bohr radius, if variable range hopping processes are significant. As a result, the electron and hole mobilities are expressed as

$$\mu_{e(h)}(E) = \mu_{e(h)}^* \exp\left[-\left(\frac{\Delta_{e(h)}}{qE\delta}\right)^{\beta}\right], \tag{10}$$

where $\mu_{e(h)}^*$ are the mobilities at large electric fields. Since the effect of electric field on carrier transport is expected to be weaker for the less localized electrons than for the holes, one expects $\Delta_h > \Delta_e$. The electric field

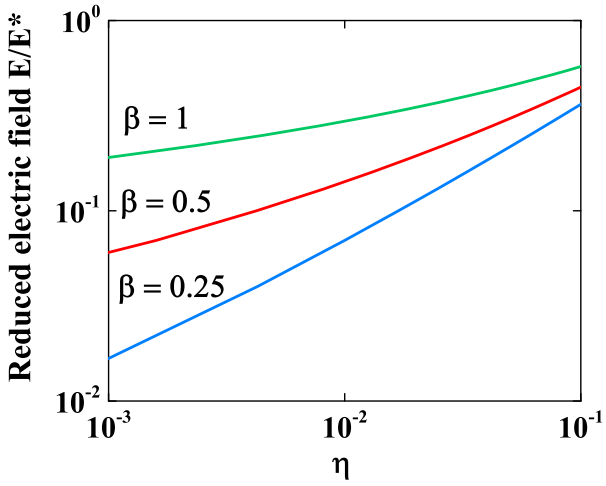


FIG. 8. Dependence of the reduced electric field as a function of η given by Eq. 11, for an exponent β, given by the thermal dependence of the conductivity, equal to 0.25 (insulating phase), 0.50 (metallic phase close to the transition) and unity.

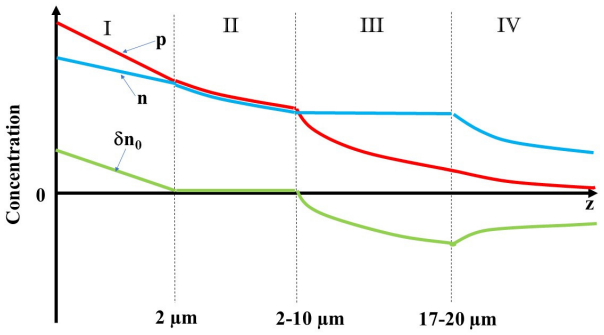


FIG. 9. Illustration of the spatial dependences of concentrations of photoelectrons n, photoholes p and of the relative concentration of intrinsic electrons δn_0 (see Sec. IV. A), for the various spatial phases defined in Fig. 2. The limits of these spatial phases depend on excitation power and their range of values is indicated. The amplitude of the Fermi sea redistribution δn_0 is negligible for an excitation power of 9 μW and increases with excitation power.

is obtained using Eq. 9 and Eq. 10 and is the solution of a nonlinear equation. In the present case where the hole drift current is smaller than the electron one ($\mu_h^* p < \mu_e^* n_0^*$), the current balance is weakly affected by the hole drift current, so that the reduced electric field $u = E/E^*$, where $E^* = \Delta_e/(q\delta)$, is the solution of $u \exp\left[-(1/u)^\beta\right] = \eta$, where

$$\eta = \frac{(D_h - D_e)\nabla p}{\mu_e^* n_0^* E^*} \approx \frac{p}{n_0^*}\frac{\mathscr{E}}{\Delta_e}\frac{\delta}{L_a} \qquad (11)$$

is the ratio of difference of diffusive currrents to the drift current of the Fermi sea in the field E^*. Note that, in a counter-intuitive way, if $D_h << D_e$, the quantity $\eta/\nabla p$ and thus the electric field, only depends on electron-related features. The approximate expression of η, found using Einstein's relation, shows that η is a fraction of unity. The dependence of the reduced electric field as a function of η for several values of β is shown in Fig. 8. For $\beta = 1/4$ which is appropriate for the insulating phase [19], the reduced electric field increases from 10^{-2} to 10^{-1} for η between several 10^{-4} and several 10^{-2}. Near the insulator-metal transition ($N_D \approx 10^{16}$ cm^{-3}), one has $\beta \approx 0.5$. The electric field becomes larger and its dependence on η becomes weaker. For the present doping level, values of β have not been reported. It is natural to expect a further increase of β, for which, as seen in Fig. 8 for $\beta = 1$, E is a significant fraction of E^* in a wide range of values of η. As a result, there occurs a self-adjustment of the electric field and therefore of the hole drift current according to Eq. 11.

C. Charge redistribution.

In the present subsection, we analyze the charge redistribution which produces the internal electric field. This charge redistribution of the photocarriers and of the Fermi sea is determined independently on models describing transport, from the spatial profiles of Fig. 7.

In order to determine the spatial profiles of the three terms of Eq. 8 separately, one defines the quantity

$$\mathscr{B} = \frac{I_{hot}}{I_{main}^2} = \mathscr{B}_0 \frac{1 - \delta n_0/p}{(1 + \delta n_0/N_D)^2} \approx \mathscr{B}_0(1 - \frac{\delta n_0}{p}) = \mathscr{B}_0 \frac{n}{p}. \qquad (12)$$

where I_{main} and I_{hot} are given by Eq. 1 and Eq. 2, respectively, $\mathscr{B}_0 = K_{hot}/[(KN_D)^2]$ and the exact expression of $\mathscr{B}$ in this equation is obtained using Eq. 8. In the same way, one defines

$$\mathscr{C} = \frac{I_{hot}}{I_{main}} = \frac{K_{hot}}{K_{main}}\frac{n}{n_0} \approx \frac{K_{hot}}{K_{main}}\frac{n}{N_D}. \qquad (13)$$

Since as shown above $n << N_D$ and $p << N_D$, one has $\delta n_0 << n_0$ because of electrical neutrality and the quantities $\mathscr{B}$ and $\mathscr{C}$ are given by their approximate expressions in Eq. 12 and Eq. 13, respectively. Thus the spatial profile of $\mathscr{C}$ reveals that of the photoelectron concentration, while that of $\mathscr{B}$ reflects the redistribution of the Fermi sea. The spatial profiles of $\mathscr{C}$ and $\mathscr{B}$, normalized to unity at $z = 0$, are shown in Curves c and d of the various panels of Fig. 7, respectively. The spatial charge redistribution obtained using their analysis is summarized in Fig. 9.

In phase II, $\mathscr{C} \approx n$ exhibits the same profile as $I_{main} \approx p$. The latter finding implies that $n \approx p$ so that $\delta n_0 << p$

and that redistribution of intrinsic electrons is negligible. One also sees that $\mathscr{B}$ is constant. Since $\delta n_0 << p$, this constant value is $\mathscr{B}/\mathscr{B}_0 \approx 1$.

This allows us to calibrate the value of $\mathscr{B}/\mathscr{B}_0$ and to determine its value at $z = 0$. In phase I, at the smallest excitation power, $\mathscr{B}$ at $z = 0$ is also close to unity. The profile of $\mathscr{C}$ coincides with that of I_{main} down to $z = 0$. Thus, in the same way as for Phase II, redistribution of the Fermi sea is negligible.

This no longer true when the excitation power increases, since $\mathscr{B}$ at $z = 0$ becomes smaller than its unit value of phase II. This implies that intrinsic electrons accumulate at the excitation spot ($\delta n_0 > 0$), and that this accumulation increases with excitation power. From the value of $\mathscr{B} \approx n/p$ at $z = 0$, we estimate that n/p takes values of ≈ 0.7, 0.5 and 0.1 for panels B, C, and D, respectively and that $\delta n_0/p$ takes complementary values of 0.3, 0.5 and 0.9, respectively.

In phase III, the constant value of $\mathscr{C}$ indicates that n is spatially constant. In the same conditions, $\mathscr{B}$ increases by about one order of magnitude, nearly independently on excitation power, implying that redistribution of intrinsic electrons is important ($\delta n_0 < 0$). Using again $\mathscr{B} \approx n/p$ one finds that for $z > 15$ μm, one has $n \approx 10p$, relatively independently on excitation power.

Finally, in phase IV, observed for $z > 17$ μm in panels C and D of Fig. 7, $\mathscr{C}$ starts to decrease, revealing, as seen from Eq. 13, a decrease of n.

In summary, the above results, illustrated in Fig. 9, show that there is a depletion of intrinsic electrons at large distance from the excitation spot, compensated by an excess near the excitation spot. The various phases in the spatial profiles are directly related with this spatial redistribution and are characterized by distinct electric field and carrier mobility values.

V. SPIN TRANSPORT ALONG THE NW

We first consider the results of Fig. 6, up to $z = 3$ μm, taken at a relatively small excitation power. At $z = 0$, the luminescence polarization is close to the maximum value of 25% without losses by spin relaxation. Upon increasing of the distance, there persists a significant S line in the difference spectrum, although no specific feature is detected in the corresponding intensity spectrum. This finding implies that, in spite of the establishment of a charge equilibrium, the photoelectrons and intrinsic electrons still form two distinct spin reservoirs. It is then assumed that each photoelectron spin reservoir, of spin $\pm$, has reached an internal equilibrium characterized by a Fermi energy $E_{F\pm}$, such that $E_{F+} + E_{F-} = 2E_F$, in order to ensure charge equilibrium [74].

For distances up to $z = 20$ μm, the spatial profiles of the polarization at the respective energies of the peaks of the line S and H lines are shown in the top panel of Fig. 7. In agreement with the known weakness of the spin relaxation processes [11], these results show for the two lines record values of the spin diffusion length, since there persists a significant polarization up to a distance of $z = 20$ μm .

For the maximum excitation power, the polarization of line H at $z = 0$ is 10%, thus smaller than for the smallest power and weakly depends on distance. We believe that the losses at at $z = 0$ are due to exchange with photoholes, which are more numerous than for the smallest excitation power (Bir Aronov Pikus mechanism [75]). The polarization of Fermi edge electrons slowly decreases with distance and is 5% for $z = 20$ μm. In order to explain these losses, it is recalled that, within the D'yakonov Perel model, the relaxation time is usually given by $1/T_1 = \Omega^2\tau_c$, where Ω is the order of magnitude of the relaxing interaction and τ_c is generally taken as the momentum relaxation time [13]. Here, for a hopping transport, it has been pointed out that relaxation only occurs during the hopping process and that τ_c is the hopping time [76]. In this case, it seems clear that τ_c should decrease with increasing excitation power, because of the increase of the characteristic energy of the electrons in the fluctuations and possibly because of screening of the fluctuations by the photocarriers. This implies that the losses by spin relaxation are smaller at high excitation power, at which τ_c is relatively small. In the same way, this model explains that the polarization losses are smaller for hot electrons, for which τ_c is smaller than for Fermi edge electrons.

VI. DISCUSSION : CHARGE TRANSPORT

In this section, we qualitatively interpret the spatial profiles in order to outline the possible mechanisms for charge transport. Note that, since the relative modification of the charge in the Fermi sea is negligible ($\delta n_0 << n_0$ so that $\delta n_0 + n_0$ is essentially spatially constant) the spatial profile of line M is mostly caused by photohole drift in the electric field E given by Fig. 8, with a typical profile for a locally homogeneous field of the type $exp(-z/L_d)$, where the drift length is $L_d = \mu_h E \tau_h$.

A. Phase I : z < 2 μm

In this spatial range the power dependence of charge redistribution can be understood using Eq. 11. Indeed, an increase of the excitation power will increase p, which will produce an increase of η and therefore of the outward electric field required by a static equilibrium between diffusive and drift currents.

B. Phase II : 2 μm < z < 2-10 μm

In this spatial range, the observation of an exponential slowly-decaying profile, up to 10 μm at low excitation power, is in agreement with the model described in

Sec. IV B, and suggests long range hole drift in the electric field obtained from Eq. 11. Since hole transport is mostly due to drift in the electric field, the above model predicts that the drift length should increase with excitation power. Indeed, an increase of p induces a increase of η as seen from Eq. 11, and thefore an increase of electric field. This is in contradiction with the observations according to which the slope of Phase I decreases with increasing excitation power.

This contradiction can be resolved since, as discussed in Appendix, the energy-distribution of holes in the fluctuations is relatively narrow, at a given nonzero kinetic energy in the fluctuations [18, 45]. It is then proposed that above a given distance, the electric field induces an increase of the hole energy, so that holes can more easily undergo tunneling processes. Such increase of the hole energy at high excitation power is evidenced from the blue shift of line M at high excitation power (see supplementary material). There results an increase of the length δ, inducing a decrease of E^* and therefore of the hole drift length with excitation power, as observed.

C. Phase III 2-10 μm $< z <$ 17-20 μm

At a distance between 2 μm and 10 μm depending on excitation power, the profile is no longer exponential and the increased value of $\vec{\nabla} p$ reveals, as seen from Eq. 9, that the electric field is increased.

We propose that, in the same way as assumed for the preceding phase, this increased electric field will further increase the average hole kinetic energy so that hopping processes have a strongly increased length, corresponding to an increase of δ. It is shown here that the onset of this phase very likely occurs when the hole average energy is large enough so that transport becomes quasi-ballistic near the top of the fluctuations. A model considering a quasi-ballistic transport between two phonon emission processes with a characteristic time τ_{ph}, explains the spatial profiles. Assuming for simplicity that the electric field E is spatially constant in this region, the hole spatial profile is of the form $p(z) \approx exp(-z/v_h\tau_{ph})$ where v_h is the hole velocity so that $v_h\tau_{ph}$ is the mean free path for phonon emission. For ballistic transport, accelerated by an electric field, one has $v_h = \sqrt{2qm_h^{*-1}Ez}$. One finally obtains

$$p(z) \approx exp(-\sqrt{z/\mathscr{L}}) \tag{14}$$

where $\mathscr{L} = 2(q/m_h^*)E\tau_{ph}^2$. As shown in Fig. 7, the spatial profiles in this phase are well approximated by Eq. 14 in view of the approximations made. Here $\mathscr{L}$ is 0.5 μm, 1.1 μm, 1.1 μm and 1.8 μm for Curves a to d and therefore slightly increases with excitation power. Using $\mathscr{L} \approx 1$ μm and $\tau_{ph} \approx 0.25$ ps [23], one finds a physically reasonable value of the internal electric field, of the order of 0.1 V/μm. This value is smaller than the unscreened electric field near the donor ($E_D/a_0^* \approx 0.6V/\mu$m).

Note that the distance corresponding to the beginning of phase III decreases with increasing excitation power. This is because in Phase II, the internal electric field increases with excitation power so that the limit kinetic energy for hole quasi ballistic transport is reached earlier.

D. Phase IV : $z > 17 - 20$ μm

The maximum distance over which photoelectrons can be transported can be found at high excitation power in panels C and D of Fig. 7. At these powers, for $z > 17\mu$m, $\mathscr{C}$ starts to decrease, revealing, as seen from Eq. 13, a decrease of n. It is concluded that photoelectrons can be transported over distances as large as 20 μm. Since no change of slope is apparent on the profile of I_{main} and since $\mathscr{B}$ also decreases in this spatial range, this suggests a decrease of $-\delta n_0$. It is thus proposed that the limit to this distance is the resulting change of local electric field.

VII. CONCLUSION

We have investigated the mechanisms of charge and spin transport in HVPE-grown, plasma-passivated GaAs NWs, at 6K and as a function of excitation power. These NWs have a n-type doping level in the low 10^{17} cm^{-3} range implying that they are metallic with a tail of density of states below the bottom of the conduction band and above the top of the valence band. The luminescence spectra exhibit several well-resolved lines, due to hot electrons, band-to-band and acceptor recombination. This exceptional quality reflects the material quality as well as the efficiency of the plasma surface passivation which was used. Using a spatially-resolved polarized lumnescence technique, we have investigated at 6K the intensity and polarization spectra as a function of distance to the excitation spot, as well the intensity and polarization spatial profiles for selected energies in the spectrum.

The main features of charge and spin transport is summarized as follows.

a) After creation and thermalization of photocarriers, a significant fraction of the photoholes is able to avoid recombination at the place of excitation, so that minority hole transport is achieved up to a distance of 20 μm.

b) Minority hole transport is achieved up to a distance of 20 μm under the effect of the large internal electric field of ambipolar origin. This field arises from the spatial redistribution of the Fermi sea, keeping an approximate charge neutrality. It has two main effects on the distribution of photocarriers. Firstly, there results a strong enhancement of charge mobility and therefore of distance travelled by the minority holes before recombination. Secondly, it is proposed that the electric field increases the average hole kinetic energy in the fluctuations, so that a transition to a quasi-ballistic regime takes place.

c) Photoelectron transport is characterized by establishment of a charge equilibrium with the Fermi sea over a distance of the order of 2 μm. These electrons remain distinct spin reservoirs, although their charges are in thermodynamic equilibrium. At large excitation power, the photoelectron spin polarization is preserved up to a record distance of 20 μm. The decrease of excitation power leads to an increase of the polarization losses. These losses are attributed to hopping relaxation. Achievement of spin transport over this record length implies that such NWs are good candidates for spintronics applications.

Appendix A: Spectral investigation of the nearbandgap photoemission spectrum

The nearbandgap normalized luminescence intensity spectra at $z = 0$ are shown in Panel A of Fig. 10 for selected excitation powers. one sees that the relative intensity of line S increases with excitation power. Curve e of Panel A shows for reference, the difference spectrum for the smallest excitation power of 9 μW.

In order to interpret these spectra, it is recalled that the luminescence properties of metallic NW depend on the statistics of electrons and photoholes. Since photoholes tend to get trapped in the potential wells, since relaxation of their kinetic energy occurs in a short characteristic time of 1 ps [23, 24], where tunneling processes are less probable because of their large effective mass, the holes cannot be described by a thermal equilibrium, but by a balance between thermalization and recombination [18, 30, 45]. As shown in Ref. [18], the hole occupation probability is obtained by a resolution in steady-state of the rate equation and is given by

$$f_v(\epsilon_v) = \frac{W_p p}{W_p p + W_n(n_0 + n)} F(E_{Fh}). \qquad \text{(A1)}$$

This quantity depends on the ratio of the capture probability W_p of a hole and of the probability W_n for recombination with electrons. Here, n and n_0 are the concentrations of photoelectrons and intrinsic electrons, p is the hole concentration and $F(E_{Fh})$ is a Fermi function of ϵ_v with E_{Fh} given by

$$E_{Fh} = k_B T_h ln\left[\frac{W_p N_v}{W_p p + W_n(n_0 + n)}\right] \approx k_B T_h ln\left[\frac{W_p N_v}{W_n n_0}\right] \qquad \text{(A2)}$$

Here N_v is the valence band effective density of states. The approximate expression is valid at low excitation power, for which $n << n_0$ and $W_p p << W_n n_0$.

Because of the dependence of the prefactor in Eq. A1 on concentration and kinetic energy, this distribution is by no means a Fermi one, while E_{Fh} should not be viewed as an effective Fermi energy. It has been proposed that, because of the large recombination probability of holes at the top of the fluctuations, the steady-state hole concentration at the top of the fluctuations is smaller than that at higher kinetic energy. Thus, the hole energy distribution is narrow and peaks at some intermediate kinetic energy in the bandtail [41, 45].

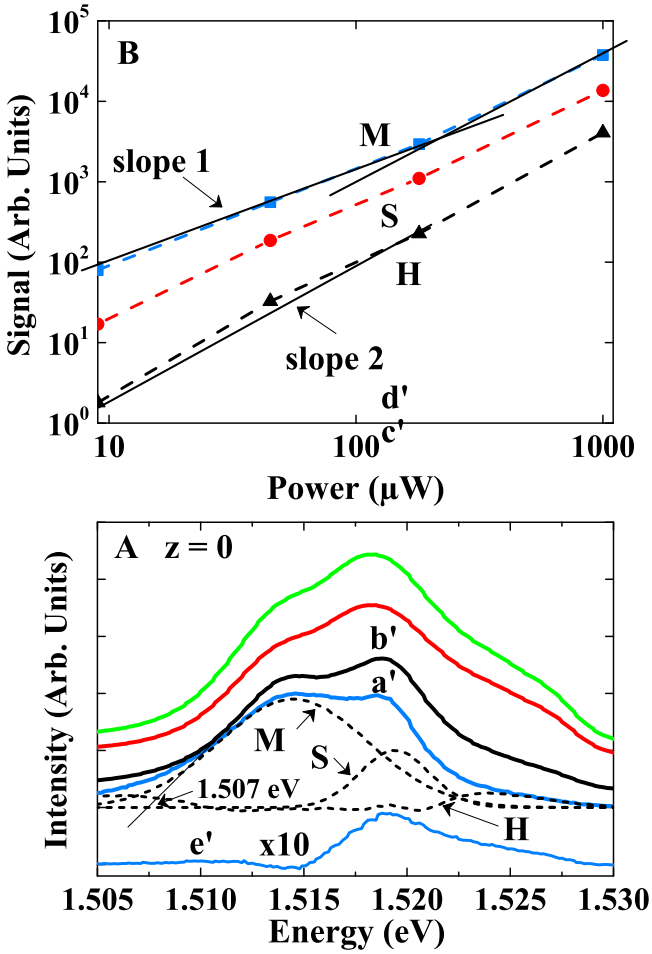


FIG. 10. Panel A shows the nearbandgap line at $z = 0$ for an excitation power of 9 μW (Curve a), of 45 μW (Curve b), 180 μW (Curve c) and 1 mW (Curve d). Curve e shows the difference spectrum (x10), given by Eq. 7 and related to the spin orientation, at an excitation power of 9 μW. The circular polarization on this spectrum is mostly limited to lines S and H, with a weak polarization on line M. Panel B shows, in logarithmic units, the power dependences of the intensities of lines M, S and H, as obtained from a decomposition of the spectra of Panel A.

The luminescence intensity at energy E of the main line, due to recombination between photoholes and intrinsic electrons, is proportional to

$$I_{main}(E) = \int_0^\infty W(\epsilon_c, \epsilon_v)\rho_c(\epsilon_c)\rho_v(\epsilon_v)f_c(\epsilon_c)f_v(\epsilon_v)d\epsilon_c. \qquad \text{(A3)}$$

with $E = E_G - \epsilon_c - \epsilon_c$ and where k-conservation does not occur because of disorder [41]. Here f_c is the electron occupation probability and $W(\epsilon_c, \epsilon_v)$ is the recombination

probability. Expressions of these quantities have been given in Ref [18], which also reports a calculation of the shape of the luminescence spectrum.

For quantitative analysis, line S was fitted by a gaussian component of half-width 2.3 meV and peak energy 1.5195 eV. The width of line S is relatively small since this line reflects the joint widths of the photoelectron distribution, determined by the temperature and of the photohole distributions which, as shown in Sec. II B, is relatively narrow. The position of line S, which corresponds to the difference between electron quasi-Fermi level and the hole energy, is found to depend very weakly on excitation power, in agreement with the expression of E_{Fh}, given by Eq. A2 at weak excitation power. For line M, one has used a gaussian shape of half width ≈ 6 meV, i. e. comparable with values measured elsewhere on Si-doped NWs [58]. Line M is broader than line S, since its width is determined by the width of the Fermi sea, of the order of the electron Fermi energy. Line M is extrapolated at low energy to a value of 1.507 eV, in relatively good agreement with the value of 1.503 eV expected from Ref. [44] for this doping level. Finally, the hot photoelectron contribution H was taken as the residual signal, obtained by subtracting components S and M from the experimental profile. The shape of this component was found to depend weakly on excitation power.

Shown in Panel B of Fig. 10 are the power dependences of the integrated intensities of lines M, S and H. As expected, the intensity of line M is proportional to the excitation power, because of the linear dependence of p on excitation power in Eq. (1) (monomolecular recombination). Conversely, that of line H is proportional to its square, since in Eq. (2), both p and n increase with excitation power (bimolecular recombination). Note that the exponent of the increase of the intensity of line S, of 1.4, is slightly smaller than the value of 2 expected from Eq. (2). This departure may be due to a power dependence of K_{hot} or to the fact that a power-dependent fraction of the photoelectrons is already incorporated into the Fermi sea at $z = 0$.

ACKNOWLEDGMENTS

This work was supported by Région Auvergne Rhône-Alpes (Pack ambition recherche; Convention 17 011236 01- 61617, CPERMMASYF and LabExIMobS3 (ANR-10-LABX-16-01). It was also funded by the program Investissements d 'avenir of the French ANR agency, by the French governement IDEX-SITE initiative 16-IDEX-0001 (CAP20-25), the European Commission (Auvergne FEDER Funds).

[1] P. Krogstrup, H. I. Jorgensen, M. heiss, O. Demichel, J. V. Holm, M. Aagesen, J. Nygard, and A. F. y Morral, Nature Photonics **7**, 306 (2013).
[2] X. Duan, Nature **421**, 241 (2003).
[3] J. W. G. van den Berg, S. Nadj-Perge, V. S. Pribiag, S. R. Plissard, E. P. A. M. Bakkers, S. M. Frolov, and L. P. Kouwenhoven, Phys. Rev. Lett. **110**, 066806 (2013).
[4] M. N. Gabriel, J. R. Kirschbrown, J. C. Christesen, C. W. Pinion, D. F. Zigler, E. M. Grumstrup, B. P. Mehl, E. E. M. Cating, J. F. Cahoon, and J. M. Papanikolas, Nanolett **13**, 1336 (2013).
[5] Y. Nagamune, H. Watabe, F. Sogawa, and Y. Arakawa, Appl. Phys. Lett. **67**, 1535 (1995).
[6] J. Bolinsson, K. Mergenthaler, L. Samuelson, and A. Gustafsson, Journal of Crystal Growth **215**, 138 (2011).
[7] A. Darbandi and S. P. Watkins, Journal of Applied Physics **120**, 014301 (2016).
[8] A. Gustafsson, J. Bolinsson, N. Sköld, and L. Samuelson, Appl. Phys. Lett. **97**, 072114 (2010).
[9] D. Spirkoska, J. Arbiol, A. Gustafsson, S. Conesa-Boj, F. Glas, I. Zardo, M. Heigoldt, M. H. Gass, A. L. Bleloch, S. Estrade, et al., Phys. Rev. B **80**, 245325 (2009).
[10] C. Gutsche, R. Niepelt, M. Gnauck, A. Lysov, W. Prost, C. Ronning, and F. Tegude, Nano Letters **12**, 1453 (2012).
[11] R. I. Dzhioev, K. V. Kavokin, V. L. Korenev, M. V. Lazarev, B. Y. Meltser, M. N. Stepanova, B. P. Zakharchenya, D. Gammon, and D. S. Katzer, Phys. Rev. B **66**, 245204 (2002).
[12] M. Romer, H. Bernien, G. Muller, D. Schuh, J. Hubner, and M. Oestreich, Phys. Rev. B **81**, 075216 (2010).
[13] M. I. D'yakonov and V. I. Perel, JETP Lett. **13**, 467 (1971).
[14] R. I. Dzhioev, B. P. Zakharchenya, V. L. Korenev, and M. N. Stepanova, Phys. Solid State **39**, 1765 (1997).
[15] A. L. Efros, Y. S. Halpern, and B. I. Shklovsky, *Proceedings of the International Conference on Physics of semiconductors, Warsaw 1972* (Polish Scientific publishers, Warsaw, 1972).
[16] B. I. Shklovskii and A. L. Efros, *Electronic Properties of Doped Semiconductors* (Springer-Verlag, Berlin, 1984).
[17] G. Borghs, K. Bhattacharyya, K. Deneffe, P. Vanmieghem, and R. Mertens, J. Appl. Phys. **66**, 4381 (1989).
[18] A. P. Levanyuk and V. V. Osipov, Sov. Phys. Uspekhi **24**, 187 (1981).
[19] M. Benzaquen, D. Walsh, and K. Mazuruk, Phys. Rev. B **36**, 4748 (1987).
[20] M. Cutler and N. F. Mott, Phys. Rev. **181**, 1336 (1969).
[21] P. W. Anderson, Phys. Rev. **1492**, 1336 (1958).
[22] C. Echeverria-Arrondo and E. Y. Sherman, Phys. Rev. B **85**, 085430 (2012).
[23] A. Chébira, J. Chesnoy, and G. M. Gale, Phys. Rev. B **46**, 4559 (1992).
[24] D. Bimberg, H. Munzel, A. Steckenborn, and J. Christen, Phys. Rev. B **31**, 7788 (1985).
[25] M. R. Ramdani, E. Gil, C. Leroux, Y. Andre, A. Trassoudaine, D. Castelluci, L. Bideux, G. Monier, C. Robert-Goumet, and R. Kupka, Nano Letters **10**, 1836 (2010).
[26] E. Gil, V. G. Dubrovskii, G. Avit, Y. Andre, C. Leroux,

K. Lekhal, J. Grecenkov, A. Trassoudaine, D. Castelluci, G. Monier, et al., Nano Letters **14**, 3938 (2014).
[27] H. Hijazi, G. Monier, E. Gil, A. Trassoudaine, C. Bougerol, C. Leroux, D. Castelluci, C. Robert-Goumet, P. Hoggan, Y. Andre, et al., Nano Letters **19**, 4498 (2019).
[28] I. Favorskiy, D. Vu, E. Peytavit, S. Arscott, D. Paget, and A. C. H. Rowe, Rev. Sci. Instr. **81**, 103902 (2010).
[29] F. Cadiz, P. Barate, D. Paget, D. Grebenkov, J. P. Korb, A. C. H. Rowe, T. Amand, S. Arscott, and E. Peytavit, J. Appl. Phys. **116**, 023711 (2014).
[30] D. Redfield, J. P. Wittke, and J. I. Pankove, Phys Rev B **2**, 1830 (1970).
[31] J.-N. Chazalviel, Phys. Rev. A **42**, 7355 (1990).
[32] W. H. Knox, D. S. Chemla, G. Livescu, J. E. Cunningham, and J. E. Henry, Phys. Rev. Lett. **61**, 1290 (1988).
[33] B. Brill and M. Heiblum, Phys. Rev. B **49**, 14762 (1994).
[34] N. I. Goktas, E. M. Fiordaliso, and R. R. LaPierre, Nanotechnol. **29**, 234001 (2018).
[35] Supplemental material I: Estimate of the NW doping level.
[36] M. Heiss, C. Colombo, and A. F. i Morral, Proceedings of SPIE **8106**, 810603 (2011).
[37] O. Demichel, M. Heiss, J. Bleuze, H. Mariette, and A. F. i Morall, Appl. Phys. Lett. **97**, 201907 (2010).
[38] H. Mehdi, F. Réveret, C. Bougerol, C. Robert-Goumet, P. E. Hoggan, L. Bideux, B. Gruzza, J. Leymarie, and G. Monier, Applied Surf. Sci. **495**, 143586 (2019).
[39] Y. André, N. I. Goktas, G. Monier, H. Mehdi, C. Bougerol, L. Bideux, A. Trassoudaine, D. Paget, J. Leymarie, E. Gil, et al., Nanoexpress **1**, 020019 (2020).
[40] H. Mehdi, G. Monier, P. E. Hoggan, L. Bideux, C. Robert-Goumet, and V. G. Dubrovskii, Applied Surf. Sci. **427**, 662 (2018).
[41] J. De-Sheng, Y. Makita, K. Ploog, and H. J. Queisser, J. Appl. Phys. **53**, 999 (1982).
[42] H. P. D. Lanyon and R. A. Tuft, IEEE trans. electron devices **26**, 1014 (1979).
[43] Since the effective diameter of the NW bulk, after removal of the surface depletion, is about 4 times the Bohr radius a_0^*, screening is rather three-dimensional. However, the TF model is only indicative since it assumes that screening only induces an energy shift of the electronic states. This approximation does not hold here since localized states can be suppressed or added by the mobile carriers. As a result, a numerical self-consistent approach is necessary in order to correctly describe the screening of the fluctuations by mobile carriers.
[44] J. R. Lowney, Journ. Appl. Phys. **60**, 2854 (1986).
[45] B. G. Arnaudov, V. A. Vil'kotskii, D. S. Domanevskii, S. K. Evtimova, and V. D. Tkachev, Sov. Phys. Semicond **11**, 1054 (1977).
[46] S. Baranovskii and O. Rubei, *Charge Transport in Disordered Materials* (Springer Handbook of Electronic and Photonic Materials, Ed. S. Kasap and P. Capper, Ch. 9, Springer-Verlag, Berlin, 2017).
[47] R. A. Smith, *Semiconductors* (Cambridge University Press, Cambridge, 1978).
[48] Supplemental material II: Resolution of the unipolar diffusion equation.
[49] D. B. Wittry and D. F. Kyser, J. Appl. Phys **38**, 375 (1967).
[50] F. Cadiz, D. Paget, A. C. H. Rowe, L. Martinelli, and S. Arscott, Appl. Phys. Lett **107**, 092108 (2015).
[51] F. Cadiz, D. Paget, A. C. H. Rowe, and S. Arscott, Phys. Rev. B **92**, 121203(R) (2015).
[52] F. Cadiz, D. Lagarde, P. Renucci, D. Paget, T. Amand, H. Carrere, A. C. H. Rowe, and S. Arscott, Appl. Phys. Lett. **110**, 082101 (2017).
[53] D. Paget, F. Cadiz, A. C. H. Rowe, F. Moreau, S. Arscott, and E. Peytavit, Journal of Applied Physics **111**, 123720 (2012).
[54] Since the NW diameter is smaller than both the excitation spot and the light absorption depth, this excitation power is equivalent to a very small effective power density of $\approx 30W/\mathrm{cm}^2$.
[55] D. W. Kisker, H. Tews, and W. Rehm, J. Appl. Phys. **54**, 1332 (1983).
[56] B. J. Skromme and G. E. Stillman, Nature **29**, 1982 (1984).
[57] J. Leymarie, *Thesis* (Universite de Nice, Nice, 1989).
[58] D. Ruhstorfer, S. Mejia, M. Ramsteiner, M. Doblinger, H. Riedl, J. Finley, and G. Koblmuller, Applied Phys. Lett. **116**, 052101 (2020).
[59] Supplemental material III: Spatial and spectral investigation of the acceptor-related emissions.
[60] R. G. Ulbrich, J. A. Kash, and J. C. Tsang, Phys. Rev. Lett. **62**, 949 (1989).
[61] C. Weisbuch, Nuovo Cimento **39B**, 660 (1977).
[62] N. Y. Lee, J. E. Kim, H. Y. park, D. H. Kwak, H. C. Leeb, and H. Lime, Solid State Commun. **99**, 571 (1996).
[63] M. Shahmohammadi, G. Jacopin, J. Levrat, E. Feltin, J. F. Carlin, J. D. Ganiere, R. Butte, N. Grandjean, and B. Deveaud, Nature Comm. **5**, 5251 (2014).
[64] E. H. Bogardus and H. B. Beeb, Phys. Rev. **176**, 993 (1968).
[65] J. Shah, R. F. Leheny, and W. Wiegmann, Phys. Rev. B **16**, 1577 (1977).
[66] G. D. Mahan, Phys. Rev. **153**, 882 (1967).
[67] F. Cadiz, D. Paget, A. C. H. Rowe, T. Amand, P. Barate, and S. Arscott, Phys. Rev. B **91**, 165203 (2015).
[68] J. A. Kash, J. C. Tsang, and J. M. Hvam, Phys. Rev. Lett. **54**, 2151 (1985).
[69] R. J. Seymour and R. R. Alfano, Appl. Phys. Lett **37**, 231 (1980).
[70] R. Binder, D. Scott, A. E. Paul, M. Lindberg, K. Henneberger, and S. W. Koch, Phys. Rev. b **45**, 1107 (1992).
[71] S. Park, D. Paget, V. L. Berkovits, V. P. Ulin, P. A. Alekseev, N. A. Kaliuzhnyi, S. A. Mintairov, and F. Cadiz, Journ. Appl. Phys. **126**, 025701 (2019).
[72] Supplemental material IV: Spatial evolution of the spectral features of the main emission line (M).
[73] C. M. Wolfe, G. E. Stillman, D. L. Spears, D. E. Hill, and F. V. Williams, J. Appl. Phys. **2**, 732 (1973).
[74] Developing the function $s \approx F(E_{F+}) - F(E_{F-})$ to first order in $E_{F+} - E_{F-}$ and dividing by the electron concentration, one finds that the polarization is proportional to $1 - F(E_F)$. The polarization spectrum in Panel D can be perfectly approximated by $1 - F(E_F)$, from which we find that the difference between the electron quasi-Fermi energy E_F and the hole energy is of 1.5195 eV. The fact that this energy coincides with the energy of line S is a further confirmation that this line is due to recombination of photoelectrons at the quasi Fermi level.
[75] G. L. Bir, A. G. Aronov, and G. E. Pikus, JETP **42**, 705 (1975).
[76] B. I. Shklovskii, Phys. Rev. B **73**, 193201 (2006).